Measurement of Dynamic Surface Tension by Mechanically Vibrated Sessile Droplets

Shuichi IWATA[*a], Satoko YAMAUCHI[a], Yumiko YOSHITAKE[b], Ryo NAGUMO[a], Hideki MORI[a], and Tadashi KAJIYA[c]

a Department of Materials Science and Engineering, Graduate School of Engineering, Nagoya Institute of Technology, Gokiso-cho, Showa-ku, Nagoya 466-8555, Japan. Tel.: +81 52 735 5256, Fax: +81 52 735 5255, E-mail: iwa@nitech.ac.jp

b Department of Mechanical Engineering, Faculty of Engineering, Nagaoka University of Technology, 1603-1 Kamitomioka, Nagaoka-shi 940-2188, Japan.

c Max Planck Institute for Polymer Research, Ackermannweg 10, 55128 Mainz, Germany.

ABSTRACT

We developed a novel method for measuring the dynamic surface tension of liquids using mechanically vibrated sessile droplets. Under continuous mechanical vibration, the shape of the deformed droplet was fitted by numerical analysis, taking into account the force balance at the drop surface and the momentum equation. The surface tension was determined by optimizing four parameters: the surface tension, the droplet's height, the radius of the droplet-substrate contact area, and the horizontal symmetrical position of the droplet. The accuracy and repeatability of the proposed method were confirmed using drops of distilled water as well as viscous aqueous glycerol solutions. The vibration frequency had no influence on surface tension in the case of pure liquids. However, for water-soluble surfactant solutions, the dynamic surface tension gradually increased with vibration frequency, which was particularly notable for low surfactant concentrations slightly below the critical micelle concentration. This frequency dependence resulted from the competition of two mechanisms at the drop surface: local surface deformation and surfactant transport towards the newly generated surface.

INTRODUCTION

Surface tension is one of the most important physical properties of liquids affecting the performance of liquid-based products[1], such as coating and spraying agents[2,3], pesticides[4], inks, and cosmetics. For many liquid-based products, surfactants are dispersed in the solvent to facilitate spreading of the liquid on the target surface and to keep the surface wet for an extended period.

In the presence of a surfactant, the surface tension of a liquid will be influenced by the dynamic process of wetting. Bleys *et al.*[5] note that when the area of the liquid surface changes rapidly, the thermodynamic equilibrium of the surfactants between the surface and bulk solution is broken. Then, surfactants diffuse from the bulk to the surface and adsorb on the surface. In the short time span from the generation of a new surface to the surfactants' attaining thermodynamic equilibrium, the surface tension varies as a function of time, owing to the depletion of the surfactants. This apparent surface tension is referred to as dynamic surface tension[6,7].

In processes that involve a rapid increase in the liquid surface area, interface phenomena are affected by the dynamic surface tension. For example, the droplet impact on a solid surface is accompanied by spreading and recoiling[8,9]. Gatne *et al.*[10] found that the maximum spreading diameter and strength of the recoiling process are governed by the dynamic surface tension variation, rather than the equilibrium surface tension. Similarly, the generation of bubbles in a surfactant solution is accompanied by the rapid emergence

of a new interface. The ease of bubble nucleation and the bubble growth rate are affected by the dynamic surface tension, which has a crucial influence on the heat transfer efficiency during the boiling of liquids[11,12].

There are several methods for measuring the dynamic surface tension, *e.g.*, the maximum bubble pressure method[13,14], the pendant-drop method[15–18], the dynamic oscillation method[19], and the jet reaction method[20]. In these methods, the interfacial area is rapidly increased at a selected rate to induce a non-uniform distribution of surfactants at the interface. However, these methods have their shortcomings. In the case of the maximum bubble pressure technique, the setup can be relatively expensive, because the pressure sensor in the bubbling system needs to have high sensitivity and high time resolution. The pendant-drop method uses a capillary and special care is required to keep it clean throughout the measurements, especially in the case of viscous liquids. A correction factor is required in order to calculate the maximum volume at the critical condition just dropping off from bottom of the capillary, which is difficult to determine for highly viscous liquids. The characteristic frequency in these methods is limited to 50 Hz owing to liquid or bubble coalescence. In addition, they typically require at least a few hundred milliliters. They are not suitable for measuring precious samples such as synthesized derivatives. Therefore, it is desirable to develop a measurement method that uses only a small amount of sample, that is easy to set up, and that can be applied to various types of liquids.

In this study, we observed droplets placed on a flat horizontal plate under a sinusoidal vibration in the vertical direction. The deformed droplet was monitored using a high-speed camera, and its shape was predicted by a statistical model under certain assumptions. The dynamic surface tension was determined by optimizing the parameters used in the analysis until the calculated droplet shape agreed well with the experimentally observed shape. This method involves a simple procedure and a simple setup. It requires only a small amount of sample solution, i.e., 1 or 2 μL for a single measurement. The effect of inertial forces can be neglected owing to the small size of the droplet. Furthermore, this method can be applied to liquids with high viscosity. Using aqueous surfactant droplets, we demonstrated how the dynamic surface tension depends on such parameters as vibration frequency, surfactant concentration, and the diffusivity of the surfactants.

EXPERIMENTAL AND THEORETICAL METHODS

Materials

Solutions of three types of water-soluble surfactants in distilled water were used, *viz*., sodium dodecyl sulfate (SDS), cetyl trimethyl ammonium bromide (CTAB), and Polyethylene Glycol-p-isooctylphenyl Ether (Triton X-100), all purchased from Wako Industries (Japan). These surfactants have different molecular weights. Their relevant physical properties at room temperature (25°C) are listed in Table 1. Each surfactant was

placed in distilled water, stirred for 24 h, and then left for an additional 24 h. Molar concentrations of these surfactants are in order of 10^{-3} mol/L, which are very dilute solutions. Therefore, the physical properties such as density, viscosity and elasticity are almost the same as those of pure water except surface tension.

Experimental Procedure and Apparatus

Figure 1 illustrates the experimental apparatus. A droplet of the sample liquid was placed on an acrylic substrate that was mounted on a vibrating platform (Wave Maker 05, Asahi Factory Corp.). The volume of the droplet was 2 μL. Prior to droplet deposition, a thin circular PVC (Polyvinyl chloride) film (2 mm in diameter, 0.1 mm in thickness) was attached to the acrylic substrate (Figure 1(b)). The droplet was deposited on the film, below which the three-phase contact line lies on the film's edge. The film's edge exhibits a large contact angle hysteresis[21], therefore, the contact line is kept pinned during the vibration cycle. The entire system was placed in a vessel under constant N_2 circulation at 25°C**.** Evaporation of the liquid sample was negligible.

Then, a sinusoidal vibration was applied to the plate. The amplitude and frequency of the vibration were controlled by a feedback control system inside the vibrating platform.

The shape of the vibrated droplet was captured by a high-speed video camera system (VW-6000 System, Keyence Co., Ltd.) from the side with a 50× close-up lens. A cold light source was placed behind the droplet to obtain an image with good contrast. The

frame rate of the high-speed camera was set at 500 fps with a shutter speed of 1/30,000 s. A set of images of the droplet was captured for several vibration cycles. The droplet image at the lowest position in the vibration cycle was extracted from the video data for use in the numerical analysis.

Methods

The mathematical analysis uses the spherical polar coordinate system (r, θ, ϕ), as shown in Figure 2. The origin is defined as the center of the three-phase contact line. The radial distance f is a function of the zenith angle θ. The contact angle is denoted by γ. Assuming quasi steady-state conditions, the equation of motion can be written as

$$\nabla p = \rho \boldsymbol{g}' \qquad (1)$$

where p is the pressure, ρ is the density of the droplet, ∇ is the gradient operator, and $\boldsymbol{g}'$ is the acceleration acting on the droplet, expressible as

$$\boldsymbol{g}' \equiv \left(g - A\omega^2 \sin \omega t \right) \boldsymbol{e}_z \quad . \qquad (2)$$

The dynamic boundary condition at the liquid-gas interface is given by the force balance

$$\boldsymbol{n}\left(p - p_G\right) + \boldsymbol{n} \cdot \left(\boldsymbol{\tau}_G - \boldsymbol{\tau}\right) + 2H\sigma\boldsymbol{n} = \boldsymbol{0} \qquad (3)$$

where $\boldsymbol{n}$ is a normal vector pointing inward, and $2H$ represents the mean curvature.

From Eqs. (1) to (3), the following third-order ordinary differential equation can be derived:

$$\frac{d}{d\theta}\left[\left\{\left(f^2+2f_\theta^2-f\,f_{\theta\theta}\right)+\left(f^2+f_\theta^2\right)\left(1-\frac{f_\theta}{f}\cot\theta\right)\right\}\Big/\left(f^2+f_\theta^2\right)^{\frac{3}{2}}\right]=(\rho g'/\sigma)(f\sin\theta-f_\theta\cos\theta) \quad , \qquad (4)$$

where f_θ represents the differential of f with respect to θ. The same notation is used in the sections titled "RESULTS AND DISCUSSION" and "CONCLUSIONS." Equation (4) can be transformed into the standard form of Eqs. (5) to (7) for numerical calculation. Ψ in Eq. (7) denotes a kind of mean curvature that is equivalent to the square brackets in Eq. (4). F is defined as $F \equiv f_\theta / f$.

$$\frac{df}{d\theta} = fF \qquad (5)$$

$$\frac{dF}{d\theta} = (1+F^2)(2-F\cot\theta) - \Psi(1+F^2)^{\frac{3}{2}} \qquad (6)$$

$$\frac{d\Psi}{d\theta} = \left(\frac{\rho g'}{\sigma}\right) f^2(\sin\theta - F\cos\theta) + \Psi F \qquad (7)$$

The following boundary conditions are applied:

$$\begin{cases} f = b \ \text{ at } \theta = 0 \\ F = 0 \ \text{ at } \theta = 0 \\ \Psi = \Psi_0 \left(\text{assumed}\right) \ \text{ at } \theta = 0 \\ f = a \ \text{ at } \theta = \pi/2 \end{cases} \qquad (8)$$

These equations can be solved by the Runge-Kutta-Gill method. The calculation starts from (f, F, Ψ) = (b, 0, Ψ_0) at $\theta = 0$ for the given parameters (a, b, σ). If a suitable Ψ_0 is provided, the final value of f is equal to the radius of the contact circle a at $\theta = \pi/2$. However, the initial value usually contains a certain level of error. Therefore, the starting value Ψ_0 should be numerically corrected by the shooting method until the fourth

boundary condition in Eq.(8), $f = a$ at $\theta = \pi/2$, is satisfied. The Regula-Falsi method is used in the correction process.

Once the shooting method is successfully applied, the objective function defined by the equation

$$E(a, b, \sigma, S) \equiv \sqrt{\frac{1}{N}\sum\left[\frac{(f_{\exp})_n - (f)_n}{(f_{\exp})_n}\right]^2} \qquad (9)$$

can be evaluated, as the summation of the root mean square of the relative errors in the droplet shape, expressible as the difference between the experimentally obtained radial distance $(f_{exp})_n$ and the simulation result $(f)_n$ at the same zenith angle θ_n. The experimental droplet coordinates are manually extracted from the video images and may thus contain a certain level of error. Therefore, we introduced an additional parameter S, referred to as the shift factor. All of the droplet coordinates are shifted from (x^i, y^i) to (x^i+S, y^i) in order to minimize the horizontal errors in the droplet coordinate data. The shift factor is determined using the simplex method.

In this study, the simplex method is also used to minimize the object function E. Figure 3 shows a flow chart of the calculation procedure. We have used two criteria for optimization process, one (ε_a) has been used in the shooting method and the other one (ε_s) has been used in the simplex method. The tolerance (ε_a) has been much strict such as 10^{-10}, because this is a simple subroutine for tuning the parameter Ψ at θ=0 to get $f = a$ (at $\theta = \pi/2$) by the shooting method. However, the tolerance for the simplex method is $\varepsilon_s = 10^{-}$

[8], which has been defined as the difference between the maximum and minimum of objective functions. The objective function at the optimum point is order of 10^{-3} as the experimental coordinates may contain a certain level of error. After the optimization process, the dynamic surface tension can be determined.

RESULTS AND DISCUSSION

Accuracy check of numerical method with a static droplet

To determine the accuracy of the numerical simulation, we used a droplet of mercury on a ZrO_2 plate under static conditions (no vibration was applied). The numerical results and droplet image are compared in Figure 4[22]. The coordinates used in the numerical prediction are plotted as filled squares. The solid line indicates the numerical results, which clearly show good agreement with the experimental results. The calculated surface tension was 482.46 mN/m (Relative standard error $E(a, b, \sigma, S)$=0.0074), which agrees well with the value from the literature, 482.1 mN/m[23].

Droplet deformation under sinusoidal vibration

After our successful experiment under static conditions, we measured a droplet on the vibrating plate. The vibration amplitude of the plate was set at 1 mm and the frequency was varied from 5 to 35 Hz. Figure 5 shows the periodic change in the droplet shape during a single cycle for 1.1 mM CTAB (*aq.*) under a vibration field (f_v = 30 Hz). The

numbers in the open squares indicate the phase in the cycle. The droplet shape changed significantly owing to the apparent gravity, while the contact line did not move during the cycle.

To compare the droplet deformation at different stages of the vibration cycle, two images of the identical droplet were superposed in Figure 6: one acquired at the highest position of the vibration (shown in blue), the other at the lowest position (shown in red). The surface of the droplet can be divided into upper and lower regions, as indicated by the dotted line (c)-(c)'. Above and below this line, bulging of the surface occurred during opposite half cycles. Assuming an axial symmetry about the vertical direction, the areas of the upper and lower surfaces can be directly calculated from the images. The results are summarized in Table 2. As the plate moved from its highest to lowest position, the lower surface area increased by 5% and the upper surface area decreased by 9%. However, the overall surface area of the droplet $S_u + S_l$ remained almost constant. This sudden local increase in surface area disrupted the uniform adsorption of surfactants on the droplet surface.

The largest change in the mean curvature of the droplet surface occurred at the lowest plate position. Therefore, in the present analysis, the dynamic surface tension was measured when the droplet was at the lowest position of the vibration. At the lowest plate position, the droplet was taken to be in a stationary state (i.e., momentarily no change in droplet shape and negligible flow inside the droplet).

Dynamic surface tension: pure liquids and surfactant solutions

Figure 7 plots dynamic surface tension vs. vibration frequency. Data for distilled water and CTAB solutions with three different concentrations are shown.

For the distilled water droplet, the calculated surface tension was independent of the vibration frequency and close to the value of 71.5 mN/m reported in the literature. We also measured the surface tension for higher-viscosity liquids (aqueous solutions of 50 wt% and 85 wt% glycerol) by the proposed method between 0 and 30 Hz. The viscosities of these samples were 5.9 mPa · s[24] and 112.9 mPa · s[25], respectively. The equilibrium surface tensions for the 50 wt% and 85 wt% glycerol solutions were 69.9 and 66.1 mN/m, respectively. These results are in good agreement with the literature, i.e., 70 mN/m for an aqueous solution of 50 wt% glycerol[24] and 66 mN/m for an aqueous solution of 85 wt% glycerol[25]. For all the pure liquids we measured, the calculated surface tensions showed no dependence on vibration frequency.

In the presence of CTAB, the situation changed entirely. Under static conditions, i.e., f_v = 0 Hz, the surface tension for a CTAB concentration of 0.5 mM was higher than that for 1.1 and 2.0 mM. The surface tension decreased with increasing CTAB concentration until it reached the critical micelle concentration (cmc), i.e., 0.96 mM.

When vibration was applied to the CTAB solution droplet, the surface tension gradually increased with vibration frequency. Vibration induces a rapid increase in surface area. On

the other hand, the adsorption of surfactants to a newly generated surface is limited by their diffusion rates. Such competition increases the dynamic surface tension. In particular, for the dilute CTAB solution droplet (0.5 mM), the surface tension reached nearly the same level as that of distilled water.

An increase in surface tension was also observed for droplets of higher CTAB concentrations (1.1 and 2.0 mM), but the increase was less marked. When the surfactant concentration was close to or higher than the cmc, sufficient amounts of surfactant monomers demicellized from micelle were present in the bulk phase adjacent to the surface, as well as in the micelle. As soon as the new surface was created, the surfactants rapidly adsorbed on it[26,27].

To investigate the effect of the molecular weight of the surfactant, we compared the dynamic surface tension of three different aqueous surfactants (Figure 8): CTAB, SDS and Triton X-100. The concentration of each surfactant solution was adjusted to be close to the cmc (1.1 mM for CTAB, 8.7 mM for SDS, and 0.33 mM for Triton-X). Although the surface tension increased with frequency in each case, the slopes were different, owing to differences in the mobility of the surfactant, which depends on its molecular weight. In general, surfactants with higher molecular weight diffuse more slowly[10]. This effect is simply evaluated by calculating the Peclet number via

$$Pe = \frac{f_V A^2}{D}, \qquad (10)$$

where A is the vibration amplitude and D is the diffusion coefficient of the surfactants.

This dimensionless number compares the rate of generation of new surface with the surfactant diffusion toward that surface. In the inset in Figure 8, the dynamic surface tension is replotted as a function of *Pe*, where the diffusion coefficients are taken from Ref. 28. A similar trend was observed for all the surfactants.

Finally, we compared our results with data from previous publications in order to verify the accuracy of our methodology. Using the maximum bubble pressure technique, Gatne et al. and Zhang et al.[10,12] investigated how the dynamic surface tension relaxes to the equilibrium surface tension as a function of the surface age τ. The surface age corresponds to the time elapsed to generate the surface and is defined as the inverse of the rate of bubble generation. Looking back at the images in Figure 5, the bulge in the surface occurs during a half cycle in which the droplet's position goes from highest to lowest. Therefore, half a vibration period (0.5 *T*) can be regarded as the characteristic time for surface generation. In Figure 9, we compare the 0.5 *T* values obtained in our measurements and the surface age τ data in Ref. 10, which yielded the same measured surface tension. In the case of CTAB, the data are well correlated and a linear dependence is obtained for all the surfactants. The slope is highest in the case of Triton X-100, which may reflect its ability to be adsorbed on the surface and its diffusion rate in the bulk liquid. These results indicate that the vibration half period is almost equivalent to the surface age measured by the maximum bubble pressure method, which verifies the accuracy and reproducibility of the present method.

CONCLUSIONS

By probing the surface deformation of a sessile droplet under mechanical vibration, we successfully developed a method for measuring the dynamic surface tension of pure liquids and aqueous surfactant solutions. Pinning the droplet at the edge of a circular film enabled stable cyclical deformation under a vibrating field. In this approach, parameter optimization was carried out until the theoretically predicted droplet shape agreed well with the experimentally observed shape. This technique requires only about 2 μL of sample solution, and can be applied to even highly viscous liquids.

Measurements were carried out for aqueous solutions of three types of surfactants with different molecular weights. The dynamic surface tension exhibited a sharp increase with vibration frequency, which depended on the surfactant concentration and molecular weight. In particular, when a fast vibration was applied to a dilute surfactant droplet, the surface tension increased, approaching that of pure water.

Our results suggest that the dynamic surface tension results from the competition of two mechanisms: the depletion of surfactants at the newly generated liquid surface due to the surface expansion and the transport of surfactants between the surface and bulk. In addition, we have confirmed that our measured value agrees well with those obtained by other available methods. In our setup, the characteristic time for surface generation corresponds to half the vibration period.

APPENDIX A

Derivation of governing equations

The governing equations can be derived from the equations for motion and force balance acting on a gas-liquid interface as follows:

A1.1 Mean curvature on the gas-liquid interface

The shape of a droplet on a flat plate is assumed to have axial symmetry about the z-axis, as shown in Figure 10. The position vector of an arbitrary point P on the interface can be expressed by the following equation in the spherical coordinate system ($(x_1, x_2, x_3) = (r, \theta, \phi)$):

$$\boldsymbol{R} = f(\theta)\boldsymbol{e}_r, \qquad \text{(A1)}$$

where θ is the polar angle, $f(\theta)$ is the radial distance of point P from the origin, and $\boldsymbol{e}_r$ is the radial unit vector.

The two tangential vectors, $\boldsymbol{g}_2$ and $\boldsymbol{g}_3$, in Figure 10 are covariant basis vectors, which can be defined with respect to the polar and azimuth directions. The covariant basis vectors $\boldsymbol{g}_i$ can be obtained through the definition $\boldsymbol{g}_i \equiv \partial \boldsymbol{R} / \partial x^i$:

$$\boldsymbol{g}_2 \equiv \frac{\partial}{\partial \theta}\left[f(\theta)\boldsymbol{e}_r \right] = f_\theta \boldsymbol{e}_r + f\, \boldsymbol{e}_\theta, \qquad \text{(A2)}$$

and $$\boldsymbol{g}_3 \equiv \frac{\partial}{\partial \phi}\left[f(\theta)\boldsymbol{e}_r \right] = f \sin\theta \boldsymbol{e}_\phi. \qquad \text{(A3)}$$

These covariant basis vectors agreed with the independent vectors defined on the surface

curve. The normal vector $\boldsymbol{n}$ can be obtained by the cross product of the covariant vectors:

$$\boldsymbol{n} = \frac{\boldsymbol{g}_3 \times \boldsymbol{g}_2}{\left|\boldsymbol{g}_3 \times \boldsymbol{g}_2\right|} = \frac{\left(f_\theta \boldsymbol{e}_\theta - f\boldsymbol{e}_r\right)}{\beta} \qquad \text{(A4)},$$

where β is defined as:

$$\beta \equiv \sqrt{f_\theta^2 + f^2} \qquad \text{(A5)}$$

The contravariant basis vectors ($\boldsymbol{g}^2$, $\boldsymbol{g}^3$) are obtained by utilizing the definitions $\boldsymbol{g}^i \cdot \boldsymbol{g}_j = \delta_j^i$ and Eqs. (A2) and (A3):

$$\boldsymbol{g}^2 = \frac{1}{\beta^2}\left(f_\theta \boldsymbol{e}_r + f\boldsymbol{e}_\theta\right); \boldsymbol{g}^3 = \frac{1}{f\sin\theta}\boldsymbol{e}_\phi \qquad \text{(A6)}$$

Therefore, the surface gradient operator ∇_s along the surface is given by the following equation:

$$\nabla_s \equiv \boldsymbol{g}^2 \frac{\partial}{\partial x^2} + \boldsymbol{g}^3 \frac{\partial}{\partial x^3} = \frac{\left(f_\theta \boldsymbol{e}_r + f\boldsymbol{e}_\theta\right)}{\beta^2}\frac{\partial}{\partial\theta} + \frac{\boldsymbol{e}_\phi}{f\sin\theta}\frac{\partial}{\partial\phi} \qquad \text{(A7)}$$

The mean curvature of the curved surface is obtained via

$$2H = -\nabla_s \cdot \boldsymbol{n}, \qquad \text{(A8)}$$

and

$$2H = -\frac{\left(f_\theta \boldsymbol{e}_r + f\boldsymbol{e}_\theta\right)\cdot \boldsymbol{n}_\theta}{\beta^2} - \frac{\boldsymbol{e}_\phi \cdot \boldsymbol{n}_\phi}{f\sin\theta}, \qquad \text{(A9)}$$

where ($\boldsymbol{n}_\theta$, $\boldsymbol{n}_\phi$) are derivatives with respect to the θ and ϕ component, respectively. They are obtained by the following equations (see Appendix C for detailed derivation):

$$\boldsymbol{n}_\theta = -\frac{1}{\beta}\left[-2 f_\theta \boldsymbol{e}_r + \left(f_{\theta\theta} - f\right)\boldsymbol{e}_\theta\right] - \frac{1}{\beta^3}\left[\left(-f\boldsymbol{e}_r + f_\theta \boldsymbol{e}_\theta\right) f_\theta \left(f + f_{\theta\theta}\right)\right] \quad \text{(A10a)}$$

$$\boldsymbol{n}_\phi = -\frac{1}{\beta}\left[f \sin\theta - f_\theta \cos\theta\right]\boldsymbol{e}_\phi \quad . \quad \text{(A10b)}$$

Substituting Eqs. (A10a), (A10b), and (A5) into Eq. (A9), we obtain

$$2H = \frac{\left[f^2 + 2 f_\theta^2 - f\, f_{\theta\theta}\right] + \left(f^2 + f_\theta^2\right)\left[1 - \frac{f_\theta}{f}\cot\theta\right]}{\left(f^2 + f_\theta^2\right)^{\frac{3}{2}}} . \quad \text{(A11)}$$

A1.2 Basic equation

A1.2.1 Force balance equation for the interface

As seen from Figure 11, we denote the total stress on the interface, deviatoric stress, pressure at the interface, and a unit tensor by $\boldsymbol{T}$, $\boldsymbol{\tau}$, p^*, and $\boldsymbol{\delta}$, respectively. The total stress tensor $\boldsymbol{T}$ for interfaces can be expressed by the following equations:

- Liquid phase interface:

$$\boldsymbol{T} = -p^* \boldsymbol{\delta} + \boldsymbol{\tau} \quad \text{(A12a)}$$

- Gas phase interface:

$$\boldsymbol{T}_G = -p_G^* \boldsymbol{\delta} + \boldsymbol{\tau}_G \quad \text{(A12b)}$$

The following three forces are acting on the interface:

- A force acting from the gas phase fluid: $\boldsymbol{T}_G \cdot \left(-\boldsymbol{n}\right)$
- A force acting from the liquid phase fluid: $\boldsymbol{T} \cdot \boldsymbol{n}$

- A surface tension force: $2H\sigma\boldsymbol{n}$

These three forces are in equilibrium at the interface:

$$\boldsymbol{T}_G \cdot (-\boldsymbol{n}) + \boldsymbol{T} \cdot \boldsymbol{n} + 2H\sigma\boldsymbol{n} = \boldsymbol{0}. \qquad \text{(A13)}$$

Substituting Eqs. (A12a) and (A12b) into Eq. (A13), and applying $\boldsymbol{\delta} \cdot \boldsymbol{n} = \boldsymbol{n}$, one obtains

$$\left(p_G^* - p^*\right)\boldsymbol{n} + \left(\boldsymbol{\tau} - \boldsymbol{\tau}_G\right) \cdot \boldsymbol{n} + 2H\sigma\boldsymbol{n} = \boldsymbol{0}. \qquad \text{(A14)}$$

Assuming a quasi-static fluid ($\boldsymbol{\tau} = \boldsymbol{\tau}_G = \boldsymbol{0}$), Eq. (A14) can be simplified:

$$\left(p_G^* - p^*\right) + 2H\sigma = 0 \qquad \text{(A15)}$$

A1.2.2 Equation of motion

The equation of motion for the liquid phase can be expressed as follows:

$$\rho \frac{D\boldsymbol{v}}{Dt} = -\nabla p + \rho \boldsymbol{g}' + \nabla \cdot \boldsymbol{\tau} \quad \text{(A16)}$$

In the case of a static fluid, by applying $\boldsymbol{v} = 0, \boldsymbol{\tau} = 0$ to Eq. (A16), we obtain

$$\nabla p = \rho \boldsymbol{g}' \qquad (1)$$

The apparent gravity vector can be defined as

$$\boldsymbol{g}' = -g' \boldsymbol{e}_z, \qquad \text{(A17)}$$

$$g' = g - A\omega^2 \sin \omega t, \qquad \text{(A18)}$$

where g is the acceleration of gravity (in the case of a static fluid, $g' = g$) and $\boldsymbol{e}_z$ is expressed in terms of the spherical coordinate system (see Appendix D for details):

$$\boldsymbol{e}_z = \cos\theta \boldsymbol{e}_r - \sin\theta \boldsymbol{e}_\theta \qquad \text{(A19)}$$

We rearrange Eq. (1) using Eq. (A19):

$$\boldsymbol{e}_r \frac{\partial p}{\partial r} + \frac{1}{r}\boldsymbol{e}_\theta \frac{\partial p}{\partial \theta} + \frac{1}{r\sin\theta}\boldsymbol{e}_\phi \frac{\partial p}{\partial \phi} = -\rho g'\left(\cos\theta \boldsymbol{e}_r - \sin\theta \boldsymbol{e}_\theta\right) \qquad \text{(A20)}$$

Thus, the following equations are obtained for each component:

$$\frac{\partial p}{\partial r} = -\rho g'\cos\theta,\ \ \frac{\partial p}{\partial \theta} = \rho g' r\sin\theta,\ \ \frac{\partial p}{\partial \phi} = 0 \qquad \text{(A21 a, b, c)}$$

As can be seen from Eq. (A21c), the pressure p is independent of the azimuth angle ϕ. Therefore, we can ignore the ϕ component, and consider only Eqs. (A21a) and (A21b).

A1.3 Introduction of the governing equation of the interface shape

As seen from Figure 12, the integral of Eq. (A21a) from point P at the interface to an arbitrary point Q in the liquid phase is

$$p = p^* - \rho g'\cos\theta\left(r - f\right) \qquad \text{(A22)}$$

Substituting Eq. (A22) into Eq. (A21b), we obtain

$$\frac{\partial p^*}{\partial \theta} - \rho g'\left(f\sin\theta - f_\theta\cos\theta\right) = 0\text{, (A23)}$$

where p^* is given by Eq. (A15):

$$p^* = p_G^* + 2H\sigma \quad . \qquad \text{(A24)}$$

The static pressure at the top of the droplet (height: b) in Figure 11 is p_0. Because of the assumption of a static fluid, we can presume the presence of a pressure head between the top of the droplet and the gas-liquid interface. This yields the equation

$$p_G^* = p_0 + \rho_G g'\left(b - f\cos\theta\right) \quad , \qquad \text{(A25)}$$

where ρ_G is the density of the gas phase. Substituting Eq. (A25) into Eq. (A24), we obtain

$$p^* = p_0 + \rho_G g'(b - f\cos\theta) + 2H\sigma. \qquad \text{(A26)}$$

By substituting Eq. (A26) into Eq. (A23), we can rearrange the terms as follows:

$$\frac{\partial(2H)}{\partial\theta} = \frac{(\rho - \rho_G)g'}{\sigma}(f\sin\theta - f_\theta\cos\theta) \quad . \quad \text{(A27)}$$

By substituting Eq. (A11) of the mean curvature into the left-hand side of Eq. (A27), the governing equations along the interface (Eq. (A28)) can eventually be obtained. In addition, because the mean curvature is a function of only the polar angle θ, we can rewrite the partial differential equation as the following ordinary differential equation:

$$\frac{d}{d\theta}\left[\frac{\left[f^2 + 2f_\theta^2 - ff_{\theta\theta}\right] + \left(f^2 + f_\theta^2\right)\left[1 - \frac{f_\theta}{f}\cot\theta\right]}{\left(f^2 + f_\theta^2\right)^{\frac{3}{2}}}\right] = \frac{(\rho - \rho_G)}{\sigma}g'(f\sin\theta - f_\theta\cos\theta), \text{(4)}$$

where we assume $\rho_G = 0$ in the body manuscript, because ρ_G is much smaller than ρ.

The boundary conditions can be taken to be as follows:

$$\text{B.C.} \quad \begin{cases} f = b \ \text{ at } \theta = 0 \\ f_\theta = 0 \ \text{ at } \theta = 0 \\ f = a \ \text{ at } \theta = \pi/2 \end{cases} \qquad \text{(A28)}$$

Appendix B

Conversion into the standard form

To convert Eq. (4) into coupled first-order ordinary differential equations, we can

introduce a new variable F:

$$F \equiv f_\theta / f \qquad \text{(B1)}$$

Thus, we can write the following equations:

$$f_\theta = fF;$$
$$f_{\theta\theta} = f_\theta F + fF_\theta = f\left(F^2 + F_\theta\right);$$
$$f^2 + f_\theta^2 = f^2\left(1+F^2\right).$$

Substituting these equations into Eq. (4), we get

$$\frac{d}{d\theta}\left[\frac{\left(1+F^2\right)\left(2-F\cot\theta\right)-F_\theta}{f\left(1+F^2\right)^{\frac{3}{2}}}\right] = \frac{\left(\rho-\rho_G\right)}{\sigma} g' f\left(\sin\theta - F\cos\theta\right). \qquad \text{(B2)}$$

We also introduce a new variable Ψ:

$$\Psi = \left[\frac{\left(1+F^2\right)\left(2-F\cot\theta\right)-F_\theta}{\left(1+F^2\right)^{\frac{3}{2}}}\right] \qquad \text{(B3)}$$

The relationship between Ψ and the mean curvature $2H$ is as follows:

$$2H = \Psi / f\,. \qquad \text{(B4)}$$

We solve Eq. (B3) in terms of F_θ and obtain

$$F_\theta \equiv \left(1+F^2\right)\left(2-F\cot\theta\right) - \Psi\left(1+F^2\right)^{\frac{3}{2}}. \qquad \text{(B5)}$$

Substituting Eq. (B3) into Eq. (B2),

$$\Psi_\theta = \frac{\left(\rho-\rho_G\right)}{\sigma} g' f^2\left(\sin\theta - F\cos\theta\right) + \Psi F\,. \qquad \text{(B6)}$$

In summary, the standard system is obtained as follows:

$$\frac{df}{d\theta} = fF \qquad (5)$$

$$\frac{dF}{d\theta} = \left(1+F^2\right)\left(2-F\cot\theta\right) - \Psi\left(1+F^2\right)^{\frac{3}{2}} \qquad (6)$$

$$\frac{d\Psi}{d\theta} = \frac{\left(\rho-\rho_G\right)}{\sigma} g'\, f^2\left(sin\,\theta - F\,cos\,\theta\right) + \Psi F \qquad (7)$$

$$\text{B.C.}\begin{cases} f = b & at \quad \theta = 0 \\ F = 0 & at \quad \theta = 0 \\ f = a & at \quad \theta = \pi/2 \end{cases} . \qquad (8)$$

Finally, by solving the first-order ordinary differential equations, it is possible to determine the droplet shape by obtaining the radius $f(\theta)$.

Appendix C

Calculation of $\left(\boldsymbol{n}_\theta, \boldsymbol{n}_\phi\right)$

When Eq. (A5), which defines β, is differentiated with respect to θ and ϕ, the following equation is obtained:

$$\beta_\theta = \frac{1}{\beta} f_\theta\left(f + f_{\theta\theta}\right); \beta_\phi = 0 \quad . \qquad (C1)$$

Differentials of the unit vectors $\left(\boldsymbol{e}_r, \boldsymbol{e}_\theta, \boldsymbol{e}_\phi\right)$ can be expressed as follows:

$$\boldsymbol{e}_{\theta,\theta} = -\boldsymbol{e}_r; \quad \boldsymbol{e}_{r,\theta} = \boldsymbol{e}_\theta; \quad \boldsymbol{e}_{r,\phi} = \sin\theta \boldsymbol{e}_\phi \; \boldsymbol{e}_{\theta,\phi} = \cos\theta \boldsymbol{e}_\phi \qquad (C2)$$

By using Eqs. (B5) and (B6), we differentiate the unit normal vector $\boldsymbol{n}$ with respect to θ and ϕ, and obtain Eqs. (A10a) and (A10b).

Appendix D

Expression of unit vector $\boldsymbol{e}_z$ in a spherical coordinate system

We define a unit vector $\boldsymbol{e}_z = A\boldsymbol{e}_r + B\boldsymbol{e}_\theta + C\boldsymbol{e}_\phi$ and find the solutions (A, B, C) to this equation. If two vectors are perpendicular to each other, the inner product of these vectors is zero. Therefore, we can calculate three inner products by applying three unit vectors in the spherical coordinate system $\left(\boldsymbol{e}_r, \boldsymbol{e}_\theta, \boldsymbol{e}_\phi\right)$ to both sides:

$$A = \boldsymbol{e}_z \cdot \boldsymbol{e}_r = \cos\theta$$

$$B = \boldsymbol{e}_z \cdot \boldsymbol{e}_\theta = \cos\left(\theta + \pi/2\right) = -\sin\theta \qquad \text{(D1)}$$

$$C = \boldsymbol{e}_z \cdot \boldsymbol{e}_\phi = \cos\left(\pi/2\right) = 0$$

Thus, we obtain

$$\boldsymbol{e}_z = \cos\theta\boldsymbol{e}_r - \sin\theta\boldsymbol{e}_\theta \qquad \text{(D2)}$$

Nomenclature

A	[m]	amplitude of vibration platform
a	[m]	radius of three-phase contact circle
b	[m]	height of liquid droplet
$\boldsymbol{e}_r$	[-]	unit vector in the r-direction
$\boldsymbol{e}_z$	[-]	unit vector in the z-direction
f	[m]	radial distance
f_v	[Hz]	vibration cycle
F	[-]	the derivative of f

g	[m/s^2]	gravitational acceleration
$\boldsymbol{g}$	[m/s^2]	gravitational acceleration vector
$2H$	[m^{-1}]	mean curvature
$\boldsymbol{n}$	[-]	normal vector
p	[Pa]	pressure
p_G	[Pa]	pressure of gas phase
r	[m]	distance from a origin point
S	[m]	horizontal origin shift
t	[s]	time
$\boldsymbol{T}$	[Pa]	total stress tensor
β	[-]	variable defined in Eq.(A5)
ϕ	[rad]	angle in spherical coordinate system
γ	[rad]	three phase contact angle defined in Fig.2
θ	[rad]	radial angle in spherical coordinate system defined in Fig.2
ρ	[kg/m^3]	density
σ	[N/m]	surface tension
τ	[s]	surface age
$\boldsymbol{\tau}$	[Pa]	deviatoric stress tensor
ω	[rad/s]	angular velocity
Ψ	[-]	variable defined in Eq.(B3)

Subscripts and Superscripts

a	Radial of three phase contact circle
s	Simplex method
G	Gas phase
H	Highest position
L	Lowest position
u	Upper side
l	Lower side

REFERECES

1 J. C. Berg, *An Introduction to Interfaces & Colloids: The Bridge to Nanoscienc*e, World Scientific (2010).

2 A. A. Tracton, *Coatings Technology Handbook*, Third Edition, CRC Press (2005).

3 B. Noziere., "The Dynamic Surface Tension of Atmospheric Aerosol Surfactants Reveals New Aspects of Cloud Activation," Nat. Commun. 5, 3335 (2014).

4 P. Berger., "Dynamic Surface Tensions of Spray Tank Adjuvants, New Concepts and Techniques in Surfactants," ACS Sym. Ser. 371, 142-150 (1988).

5 G.Bleys, "Adsorption Kinetics of Bolaform Surfactants at the Air/Water Interface," J. Phys. Chem., 89, 1027-1032 (1985).

6 Hermann Lange, “DYNAMIC SURFACE TENSION OF DETERGENT SOLUTIONS AT CONSTANT AND VARIABLE SURFACE AREA,” J. Colloid Sci., 20, 50-61 (1965).

7 Milton J. Rosen, *SURFACTANT AND INTERFACIAL PHENOMENA*, John Wiley & Sons, Inc., 3rd ed. (2004).

8 X. Zhang, “Dynamic Surface Tension Effects in Impact of a Drop with a Solid Surface,” J. Colloid and Int. Sci., 187, 166-178 (1997).

9 N.Mourougou-Candoni, “Influence of Dynamic Surface Tension on the Spreading of Surfactant Solution Droplets Impacting onto a Low-Surface-Energy Solid Substrate,” J. Colloid and Int. Sci., 192, pp.129-141 (1997).

10 Gatne, K.P., “Surfactant-Induced Modification of Low Weber Number Droplet Impact Dynamics,” Langmuir, 25(14), 8122-8130 (2009).

11 Zhang, J., “Effect of Ethoxylation and Molecular Weight of Cationic Surfactants on Nucleate Boiling in Aqueous Solutions,” J. Heat. Transfer, 126, 34-42 (2004).

12 Zhang, J., “Additive Adsorption and Interfacial Characteristics of Nucleate Pool Boiling in Aqueous Surfactant Solutions,” J. Heat. Transfer, 127, 684-691 (2005).

13 Sugden, S., “XCVII.-The Determination of Surface Tension from the Maximum Pressure in Bubbles,” J. Chem. Soc., 121, 858-866 (1922).

14 Mysels, K. J., “The Maximum Bubble Pressure Method of Measuring Surface Tension, Revisited,” Colloids and Surfaces, 43, 241-262 (1990).

15 Ferguson, A., “On the measurement of the surface tension of a small quantity of liquid,”

Proceedings of the Physical Society of London, 36, 37-44 (1923).

16 Garanet, J. P., “Considerations on the Pendant Drop Method: A New Look at Tate’s Law and Harkins’ Correction Factor,” J. Colloid and Interface Sci., 165, 351-354 (1994).

17 del Rio, O., I., “Axisymmetric Drop Shape Analysis: Computational Methods for the Measurement of Interfacial Properties from the Shape and Dimensions of Pendant and Sessile Drops,” J. Colloid and Interface Sci., 196, 136-147 (1997).

18 A. Bonfillon, “Dynamic Surface Tension of Ionic Surfactant Solutions,” J. Coll. Int. Sci., 168, 497–504 (1994).

19 Neus, L., “Dynamic Properties of Cationic Diacyl-Glycerol-Arginine-Based Surfactant / Phospholipid Mixtures at the Air / Water Interface,” Langmuir, 26(4), 2559-2566 (2009).

20 Hasegawa, T., “A Simple Method for Measuring Elastic Stresses by Jet Thrust and Some Characteristics of Tube Flows,” J. Soc. Rheology, Japan, 31(4), 243-252 (2003).

21 Gibbs, J. W., *Scientific Papers*, Dover Reprint (Dover, New York, 1961), Vol. 1, p. 326.

22 Iwata, S., “Measurement of Surface Tension and Contact Angle by Analysis of Force Balance along a Bubble/Droplet Surface,” Kagaku Kogaku Ronbunshu, 36(5), 441–448 (in Japanese) (2010).

23 M. E. Nicholas, “The effect of various gases and vapors on the surface tension of mercury,” J. Phys. Chem., 65 (8), pp 1373–1375 (1961)

24 Regan Crooks, “The role of dynamic surface tension and elasticity on the dynamics of

drop impact," Chem. Eng. Sci., 56, 5575-5592 (2001).

25 Xiaoguang Zhang, "Measurement of synamic Surface Tension by a Growing Drop Technique," J. Colloid and Interface Sci., 168, 47-60 (1994).

26 E. Tllaerts and P. Joos, "Rate of Demicellization from Dynamic Surface Tensions of Micellar Solutions," J. Phys. Chem, 86, 3471-3478 (1982).

27 Xiaohong Cui,"Mechanism of Surfactant Micelle Formation," Langmuir 2008, 24, 10771-10775 (2008).

28 Mark A. Hink, "Dynamics of Phospholipid Molecules in Micells: Characterization with Fluorescence Correlation Spectroscopy and Time-Resolved Fluorescence Anisotropy," Langmuir, 15, 992-997 (1999).

Acknowledgements

This study was partially supported by JST "Intellectual Property Utilization Support Program (Grant No. HWY2012-1-177)." We thank Mr. Fumihiko Nakamura and Mr. Hironori Suzuki for their assistance in carrying out many experiments and numerical analyses.

Table 1. Physical properties of surfactants

Surfactant	Ionic nature	MW[-]	cmc.[mM]
SDS	Anionic	288.3	~8.67
CTAB	Cationic	364.5	~0.96
Triton X-100	Nonionic	624(av.)	~0.321

Table 2. Surface areas at highest and lowest plate positions (1.1 mM CTAB aq. under a vibration field (f_v = 30 Hz))

	Upper surface area S_u [mm^2]	Lower surface area S_l [mm^2]	Total S_u+S_l [mm^2]
Highest Position(H)	S_{Hu} 2.02	S_{Hl} 7.49	S_H (S_{Hu}+S_{Hl}) 9.51
Lowest Position(L)	S_{Lu} 1.83	S_{Ll} 7.83	S_L (S_{Lu}+S_{Ll}) 9.66
Ratio S_L/S_H	S_{Lu}/S_{Hu} 0.91	S_{Ll}/S_{Hl} 1.05	S_L/S_H 1.02

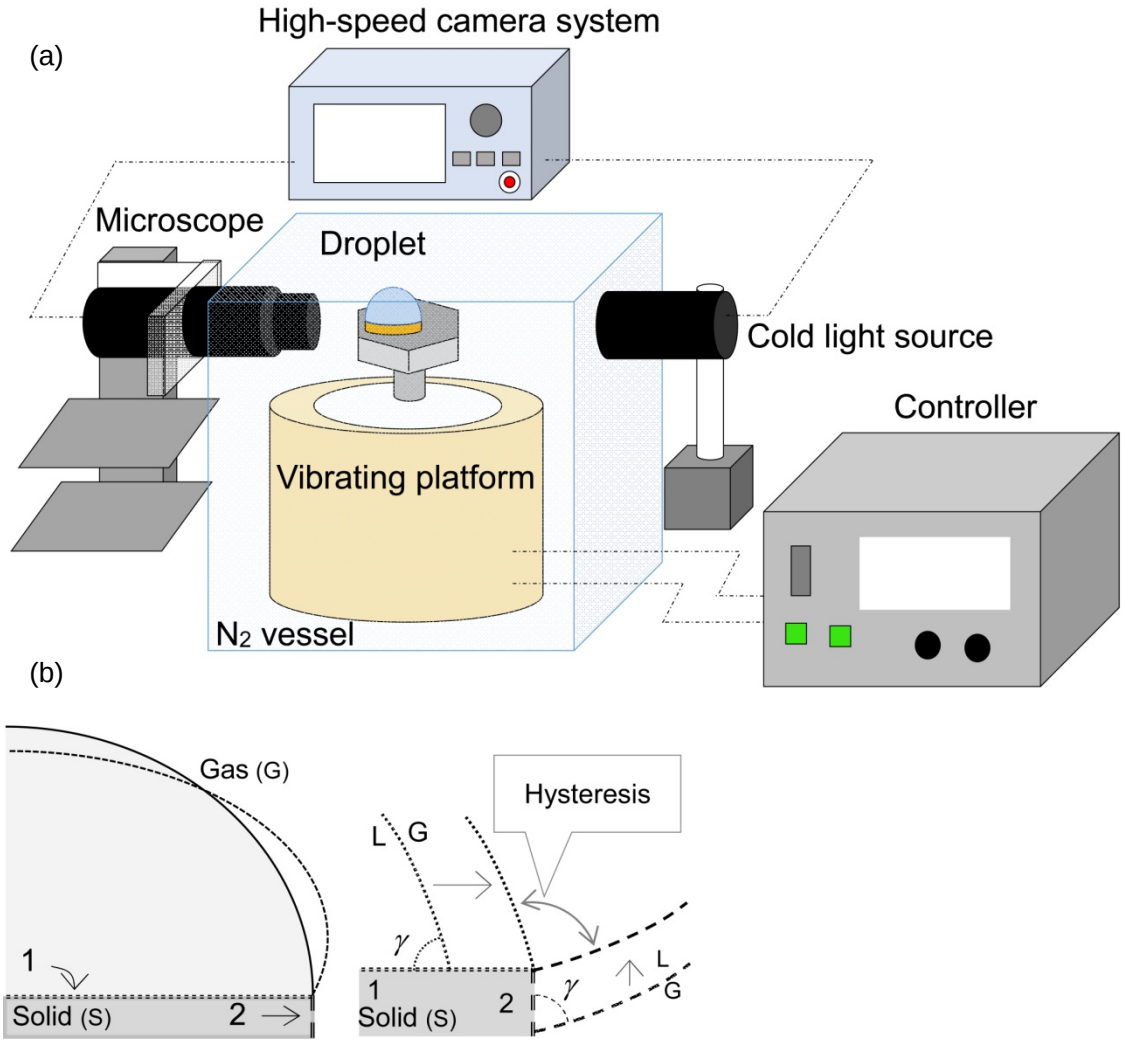

FIG. 1(a). Schematic of the experimental apparatus. A sessile drop is placed on an acrylic plate mounted on a vibration platform under N_2 atomosphere. While applying mechanical vibration, the shape of the droplet is monitored using a high-speed camera (500 fps).

(b) Detailed schematic of the substrate and droplet deposition. A circular PVC film was attached onto an acrylic plate; then, the droplet was deposited on that film. The three-phase contact line is located on the film's edge, therefore, the large contact angle hysteresis keeps the contact line immobile during the vibration cycle.

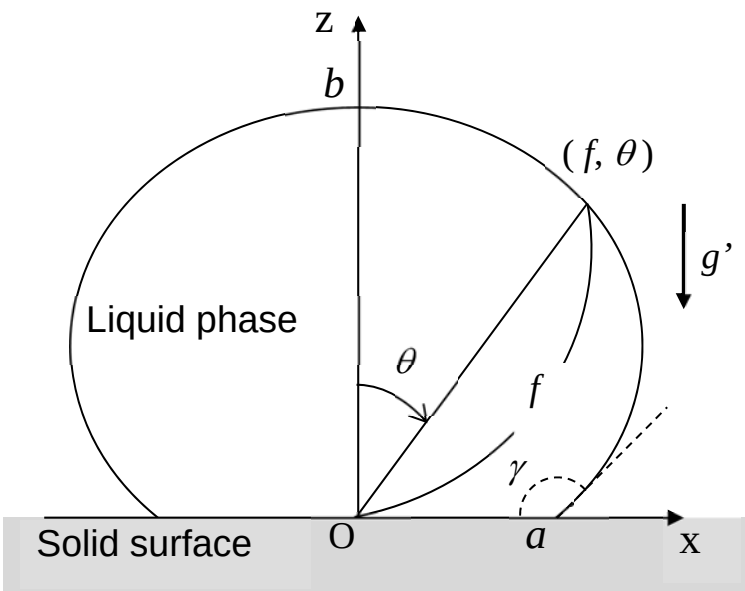

FIG. 2. Geometry and coordinates of the droplet used in the numerical analysis.

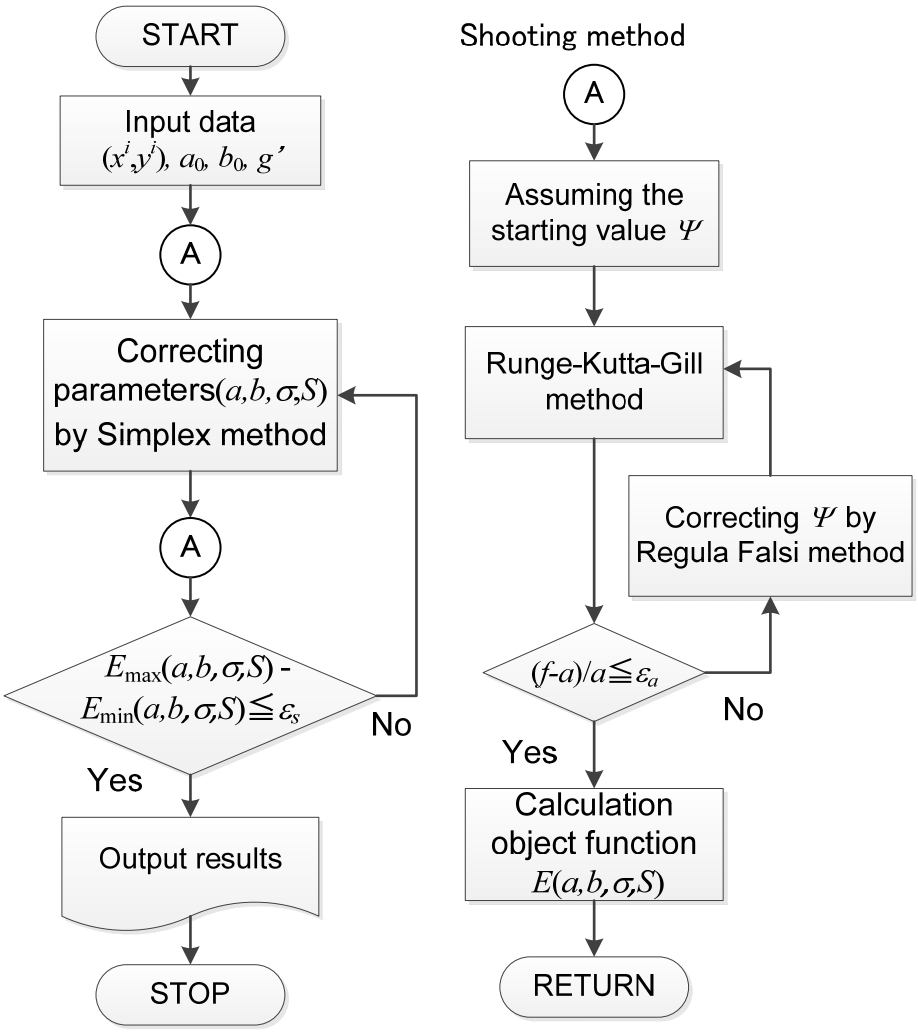

FIG. 3. Calculation flow chart.

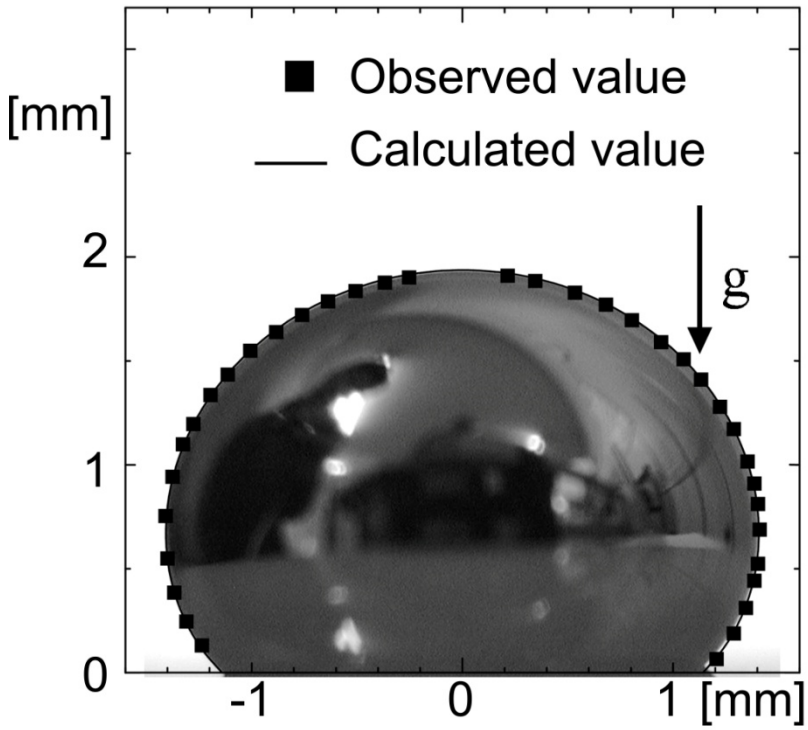

FIG. 4. Comparison of the observed profile of a static sessile droplet (Mercury/ZrO_2 at 24.0°C) and the numerically predicted profile.

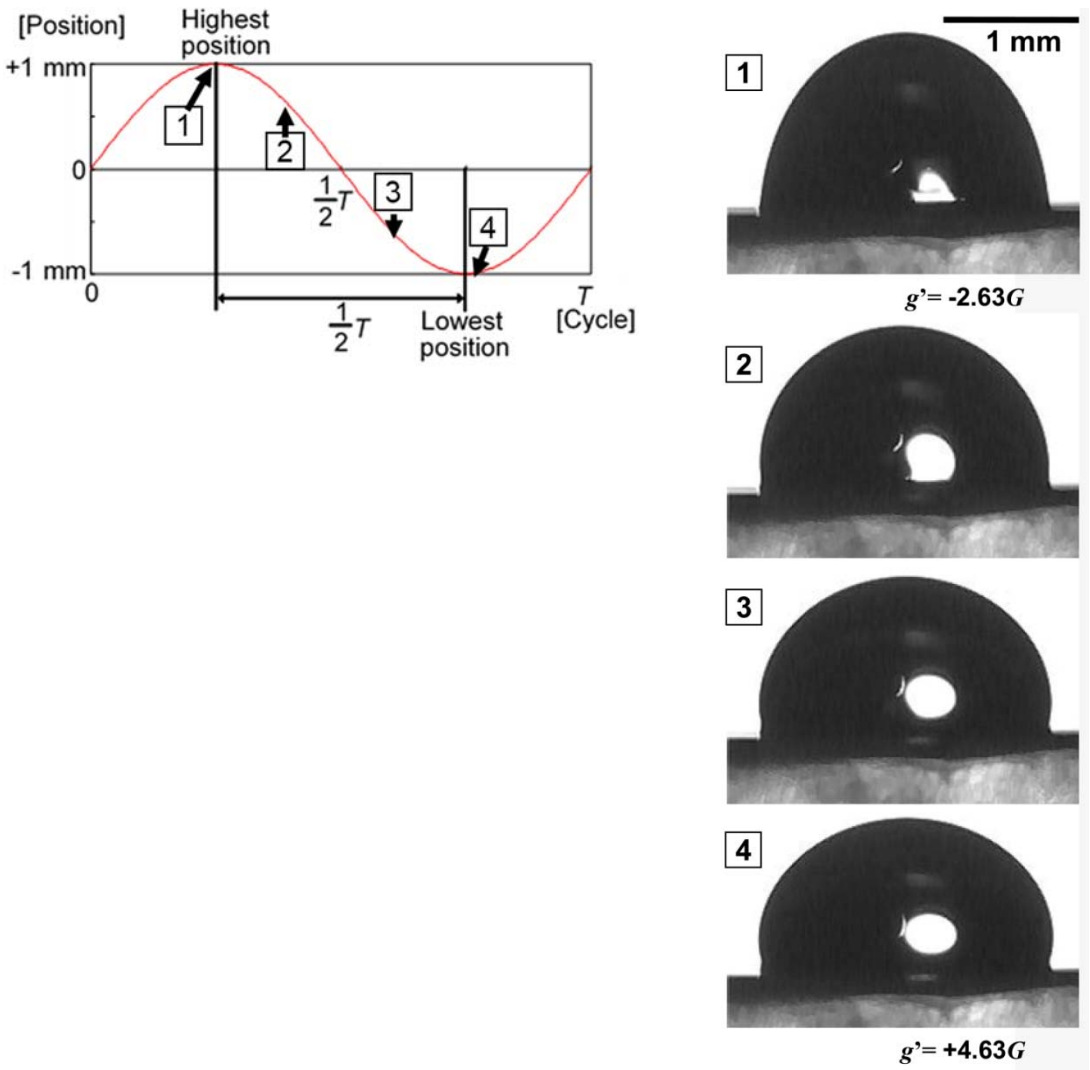

FIG. 5. Periodic change in the droplet shape during a single vibration cycle (f_v = 30 Hz). A droplet of 1.1 mM CTAB solution was used. The droplet shape changes owing to the variation in the apparent gravity *g'*.

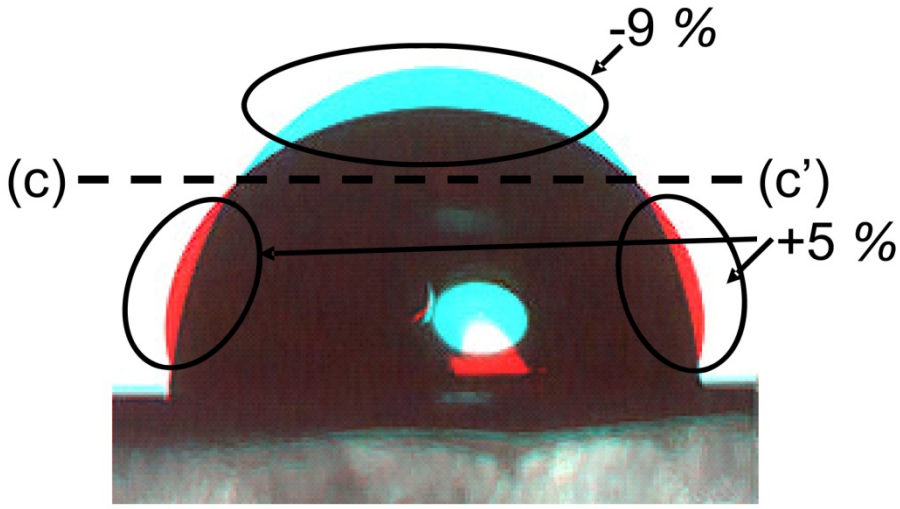

FIG. 6. Superposed images of the same droplet at different stages of the oscillation. The blue image corresponds to the drop's highest position, while the red image corresponds to its lowest position. The surface area increase and decrease are indicated in the upper and lower sections. (1.1 mM CTAB *aq*. under a vibration field (f_v = 30 Hz))

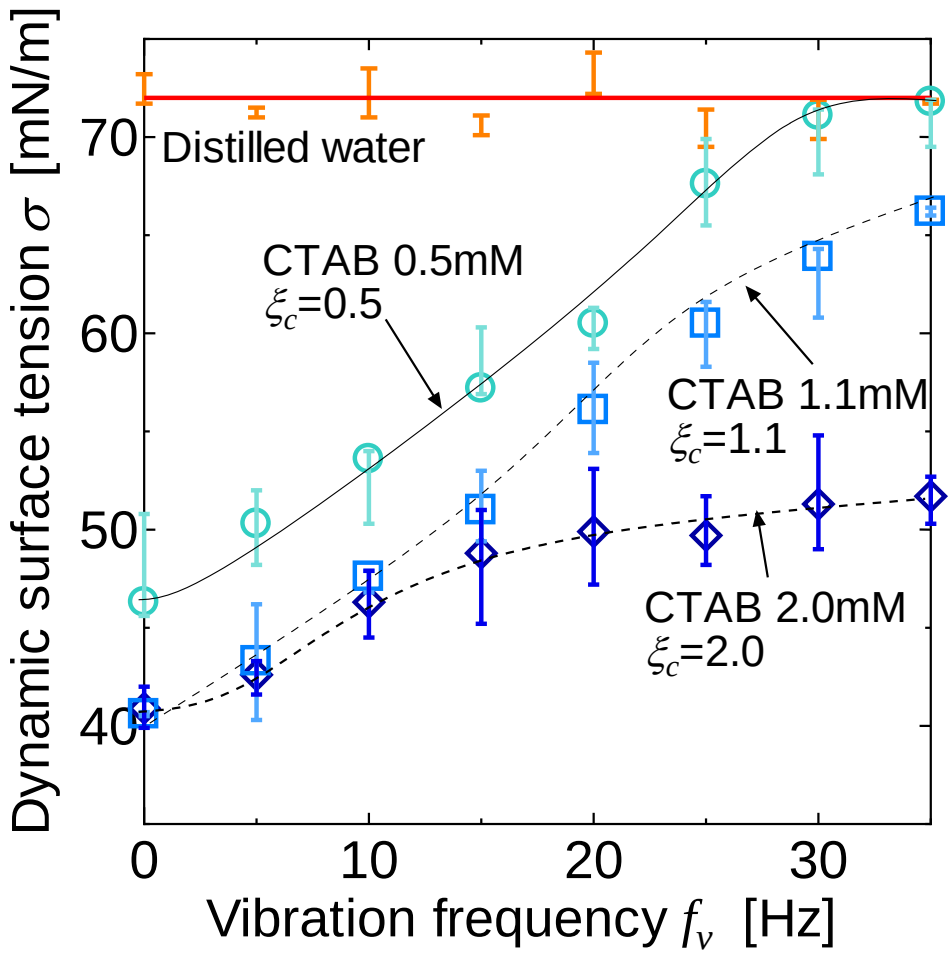

FIG. 7. Dynamic surface tension as a function of vibration frequency. Data for distilled water and CTAB solutions with three different concentrations are plotted. ξ denotes the normalized concentration, C/cmc. 6 to 8 images were averaged for each data point.

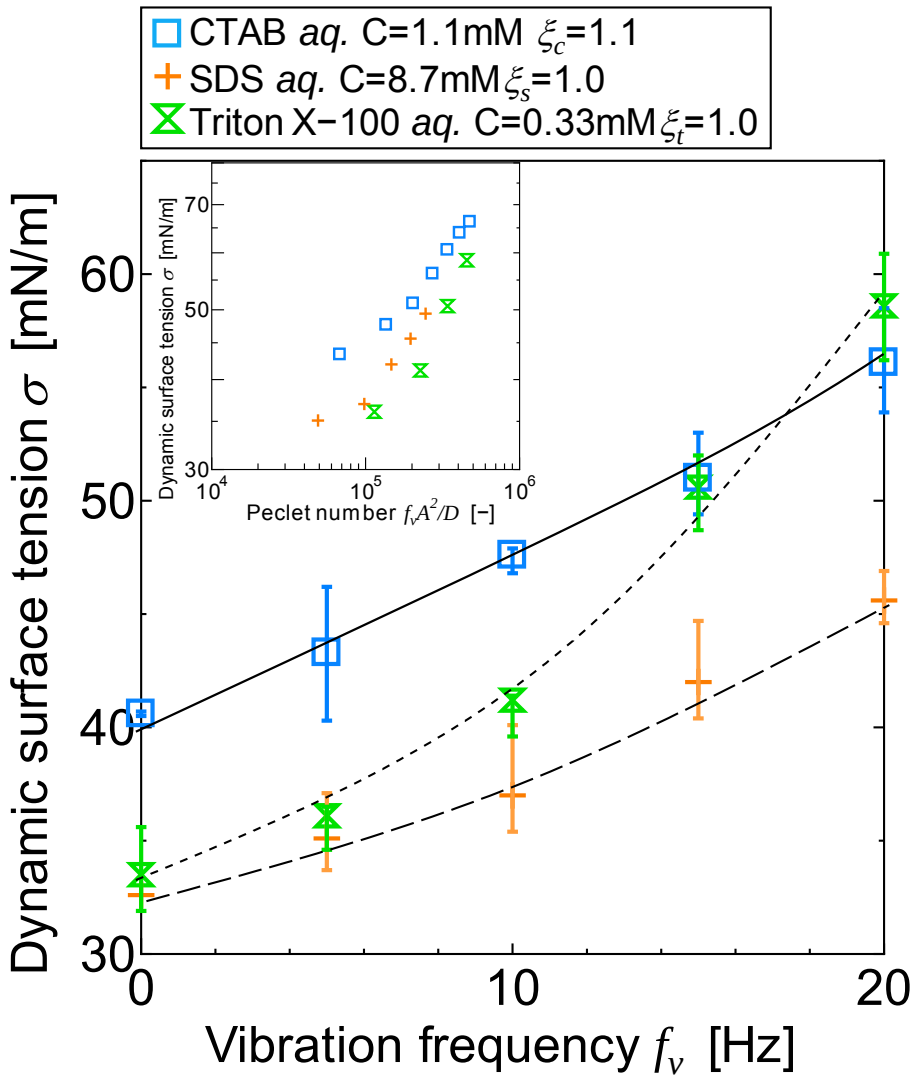

FIG. 8. Effect of molecular weight of surfactant on dynamic surface tension. 6 to 8 images were averaged for each data point.

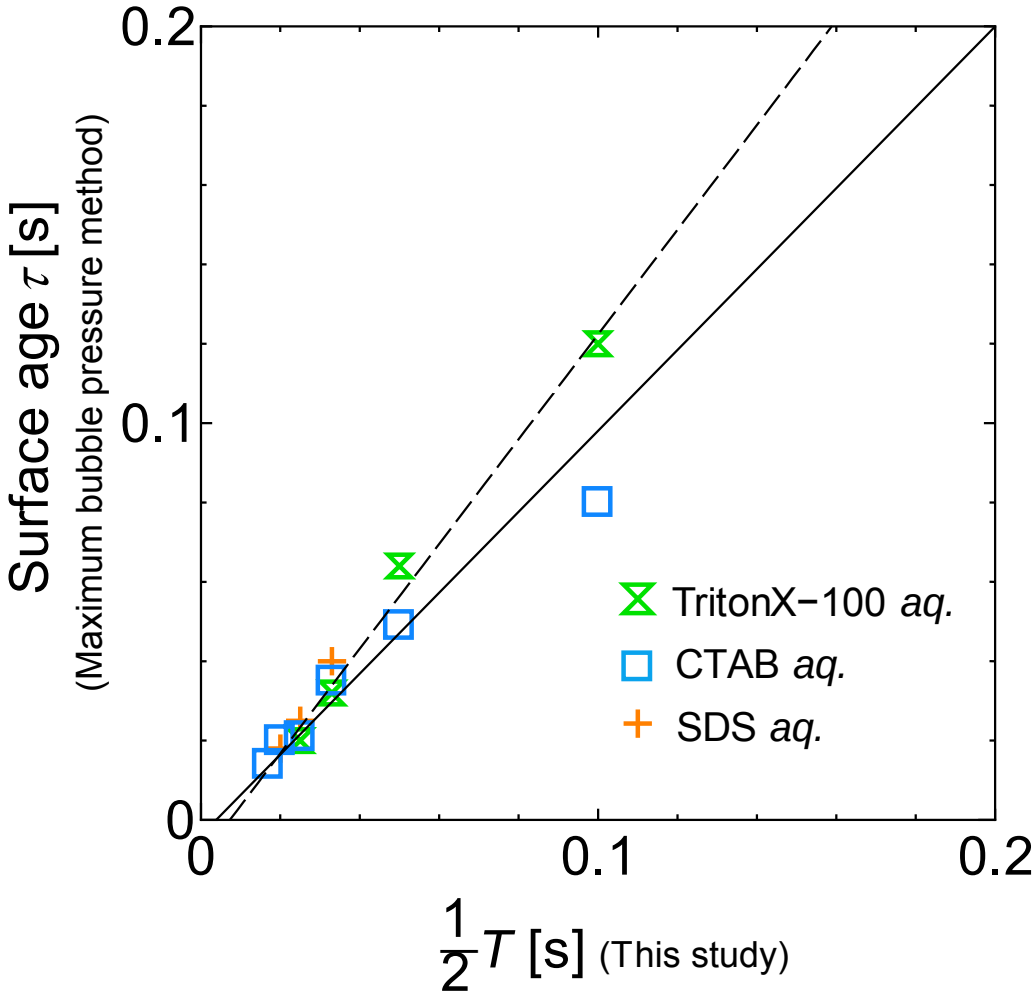

FIG. 9. Relationship between half the vibration period 1/2 T and surface age parameter τ (data are taken from Gatne et al.[10]) which yields the same value for the surface tension.

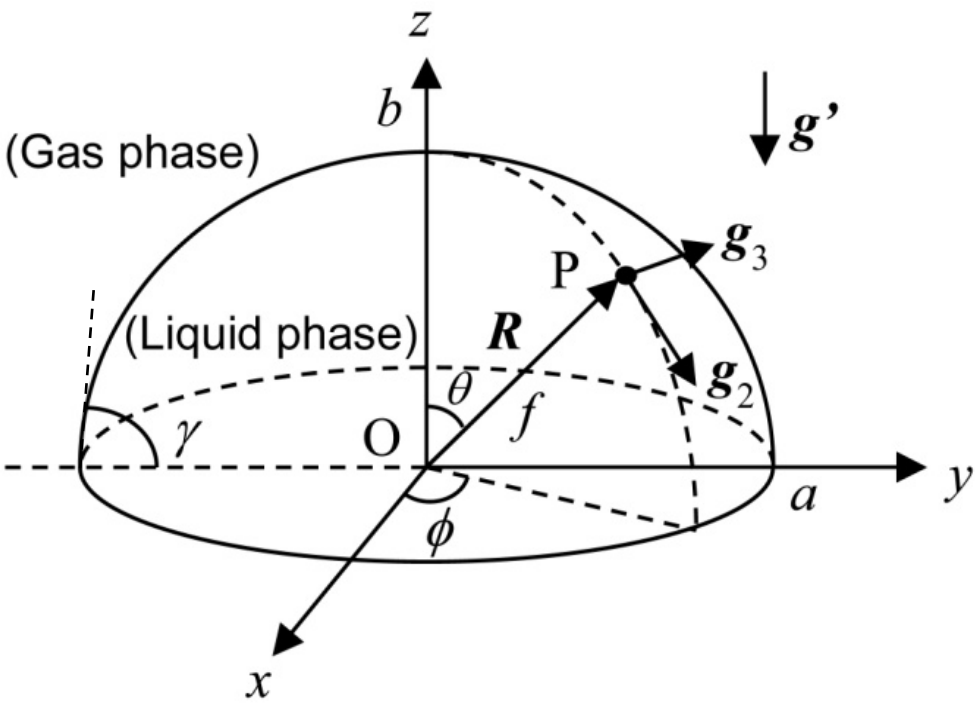

FIG. 10. A droplet in the coordinate system.

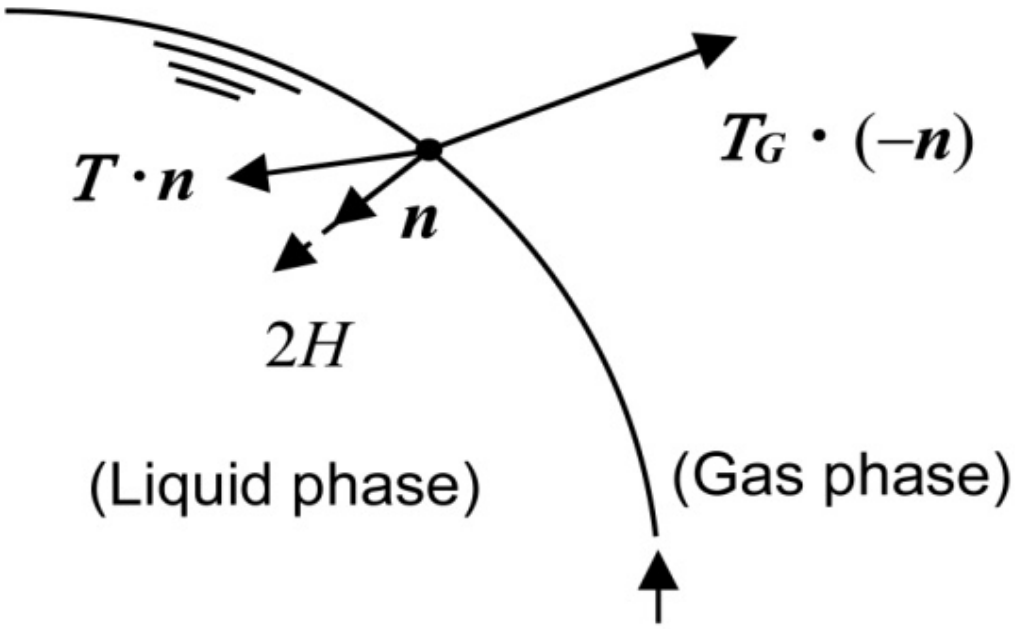

FIG. 11. Three kinds of forces acting on the gas-liquid interface.

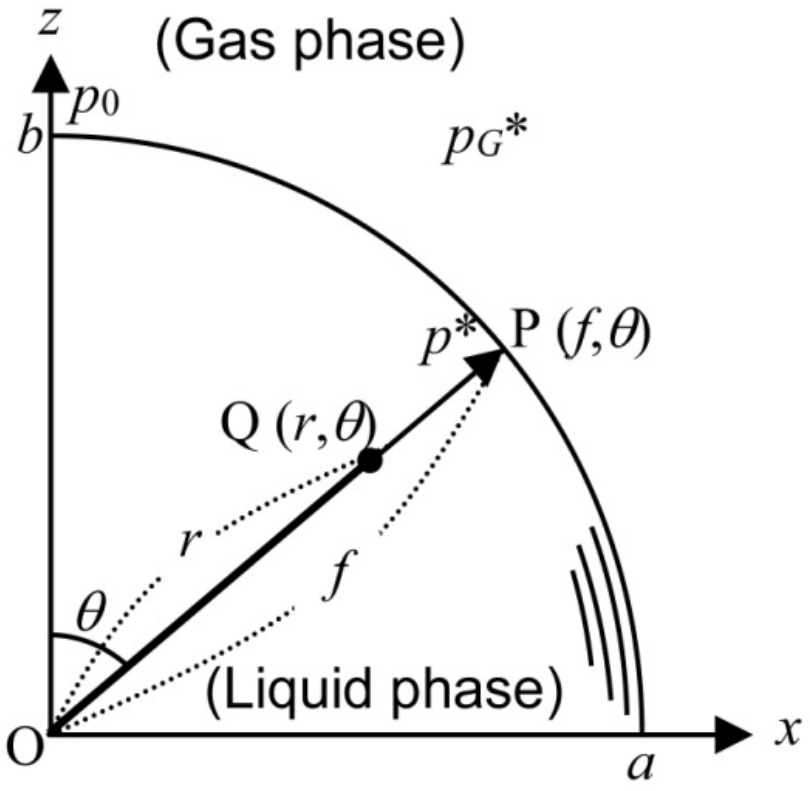

FIG. 12. Integration over the interval [*f*, *r*]